

## Article

# Theoretical Prediction of Structural, Mechanical, and Thermophysical Properties of the Precipitates in 2xxx Series Aluminum Alloy

Xuwei Fang <sup>1</sup>, Yefei Li <sup>1</sup>, Qiaoling Zheng <sup>1</sup>, Jianye Guo <sup>1</sup>, Yanmei Yang <sup>1</sup>, Weiyun Ding <sup>2,\*</sup>, Chunhui Ma <sup>2</sup>, Ke He <sup>2</sup>, Ningning Su <sup>2</sup>, Jingyi Jiang <sup>2</sup>, Xiaoxue Chen <sup>2</sup> and Haoran Wang <sup>2</sup>

<sup>1</sup> National Innovation Institute of Additive Manufacturing, Xi'an 710065, China

<sup>2</sup> China National Heavy Duty Truck Group Co., Ltd., Jinan 250000, China

\* Correspondence: dingwy@sinotruk.com

**Abstract:** We presented a theoretical study for the structural, mechanical, and thermophysical properties of the precipitates in 2xxx series aluminum alloy by applying the widely used density functional theory of Perdew-Burke-Ernzerhof (PBE). The results indicated that the most thermodynamically stable structure refers to the Al<sub>3</sub>Zr phase in regardless of its different polymorphs, while the formation enthalpy of Al<sub>5</sub>Cu<sub>2</sub>Mg<sub>8</sub>Si<sub>6</sub> is only -0.02 eV (close to zero) indicating its metastable nature. The universal anisotropy index of  $A^U$  follows the trend of: Al<sub>2</sub>Cu > Al<sub>2</sub>CuMg ≈ Al<sub>3</sub>Zr\_D0<sub>22</sub> ≈ Al<sub>20</sub>Cu<sub>2</sub>Mn<sub>3</sub> > Al<sub>3</sub>Fe ≈ Al<sub>6</sub>Mn > Al<sub>3</sub>Zr\_D0<sub>23</sub> ≈ Al<sub>3</sub>Zr\_L1<sub>2</sub> > Al<sub>7</sub>Cu<sub>2</sub>Fe > Al<sub>3</sub>Fe<sub>2</sub>Si. The thermal expansion coefficients (TECs) were calculated based on Quasi harmonic approximation (QHA); Al<sub>2</sub>CuMg shows the highest linear thermal expansion coefficient (LTEC), followed by Al<sub>3</sub>Fe, Al<sub>2</sub>Cu, Al<sub>3</sub>Zr\_L1<sub>2</sub> and others, while Al<sub>3</sub>Zr\_D0<sub>22</sub> is the lowest one. The calculated data of three Al<sub>3</sub>Zr polymorphs follow the order of L1<sub>2</sub> > D0<sub>23</sub> > D0<sub>22</sub>, all of them show much lower LTEC than Al substance. For multi-phase aluminum alloys, when the expansion coefficient of the precipitates is quite different from the matrix, it may cause a relatively large internal stress, or even produce cracks under actual service conditions. Therefore, it is necessary to discuss the heat misfit degree during the material design. The discrepancy between  $\alpha$ -Al and Al<sub>2</sub>CuMg is the smallest, which may decrease the heat misfit degree between them and improve the thermal shock resistant behaviors.

**Keywords:** aluminum; mechanical property; anti-compressibility; precipitates; thermal expansion



**Citation:** Fang, X.; Li, Y.; Zheng, Q.; Guo, J.; Yang, Y.; Ding, W.; Ma, C.; He, K.; Su, N.; Jiang, J.; et al. Theoretical Prediction of Structural, Mechanical, and Thermophysical Properties of the Precipitates in 2xxx Series Aluminum Alloy. *Metals* **2022**, *12*, 2178. <https://doi.org/10.3390/met12122178>

Academic Editors: Frank Czerwinski and Talal Al-Samman

Received: 20 November 2022

Accepted: 14 December 2022

Published: 17 December 2022

**Publisher's Note:** MDPI stays neutral with regard to jurisdictional claims in published maps and institutional affiliations.



**Copyright:** © 2022 by the authors. Licensee MDPI, Basel, Switzerland. This article is an open access article distributed under the terms and conditions of the Creative Commons Attribution (CC BY) license (<https://creativecommons.org/licenses/by/4.0/>).

## 1. Introduction

2xxx series aluminum alloys are widely used in spacecraft parts, engine pistons, aircraft structures, missile components, propellers, aircraft skeletons, etc. The 2xxx series aluminum alloys mainly include Al-Cu, Al-Cu-Mg, Al-Cu-Mg-Mn-Zr alloys, etc., which could be strengthened by heat treatment, and thereby the hardness and strength will be further improved after solutionizing treatment and the following artificial aging treatment [1–3]. The 2xxx series aluminum alloy, in particular, keeps good performance at high temperatures and is commonly used in weldable forgings and structural parts.

During artificial aging treatment of 2xxx series aluminum alloys, etc., a succession of precipitates is developed from the supersaturated solid solution of  $\alpha$ -Al.  $\theta$ -Al<sub>2</sub>Cu, is obtained from the supersaturated solid solution, and then goes through the GP zone (Guinier-Preston zone), then the metastable  $\theta''$ ,  $\theta'$  and finally the  $\theta$ -Al<sub>2</sub>Cu phase;  $S$ -Al<sub>2</sub>CuMg undergoes a similar process to  $\theta$ -Al<sub>2</sub>Cu [2]. Zr and Mn are also frequently used to improve the strength of the alloys by forming intermetallics such as Al<sub>3</sub>Zr, Al<sub>20</sub>Cu<sub>2</sub>Mn<sub>3</sub>, and Al<sub>6</sub>Mn. Particularly, Si and Fe elements are impurities in aluminum alloys, which exist as Al<sub>3</sub>Fe, Al<sub>3</sub>Fe<sub>2</sub>Si, Al<sub>5</sub>Cu<sub>2</sub>Mg<sub>8</sub>Si<sub>6</sub>, and Al<sub>7</sub>Cu<sub>2</sub>Fe.

For  $\theta$ -Al<sub>2</sub>Cu and  $S$ -Al<sub>2</sub>CuMg phases, a lot of experimental work has been conducted to reveal their microstructures, mechanical and physical properties. Kairy et al. [4] claimed

the hardness of the 2xxx series alloy can be increased with Sc and Zr additions. The fine spherical  $\text{Al}_3(\text{ScZr})$  effectively retards the recrystallization process, which benefits the high-temperature mechanical property of aluminum alloys. Actually, the ground state of  $\text{Al}_3\text{Zr}$  has a tetragonal  $\text{D}_{023}$  structure, while the  $\text{L}_{12}$  structure can be stabilized by Cu or Mn [5].  $\text{Al}_{20}\text{Cu}_2\text{Mn}_3$  is a kind of common dispersoid in 2xxx series aluminum alloys, which is formed during the homogenization [6].

The high temperature mechanical strength of aluminum alloys can be improved by fine and uniformly distributed  $\text{Al}_{20}\text{Cu}_2\text{Mn}_3$  particles [7].  $\text{Al}_{20}\text{Cu}_2\text{Mn}_3$  has an orthorhombic structure with the space group of  $\text{Bbmm}$  [8]. Shen et al. [9] reported the atomic arrangement of the  $\text{Al}_{20}\text{Cu}_2\text{Mn}_3$  structure; and the optimized lattice parameters were estimated as  $a = 23.98 \text{ \AA}$ ,  $b = 12.54 \text{ \AA}$ , and  $c = 7.66 \text{ \AA}$ . Huang et al. [10] reported  $\text{Al}_6\text{Mn}$  is less steady than  $\text{Al}_3\text{Fe}$  or  $\text{Al}_3\text{Fe}_2\text{Si}$  from the energetic point of view. Zhu et al. [11] found a high-strength die-cast aluminum alloy by optimizing the synergistic strengthening of  $Q\text{-Al}_5\text{Cu}_2\text{Mg}_8\text{Si}_6$  and  $\theta\text{-Al}_2\text{Cu}$  phases, the yield strength of 225 MPa and elongation of 4.3% were obtained. For the  $\text{Al}_7\text{Cu}_2\text{Fe}$  phase, Tian et al. [12] reported the bulk, shear and young's moduli are 107.8, 74.5, and 181.7 GPa, respectively.

Although many investigations associated with precipitates have been performed in previous experimental and theoretical work, most of them are mainly focused on the structures and mechanical strength. To date, little information is available about the thermodynamical stability, anisotropic mechanical property, temperature dependence thermal expansion, and thermal capacity due to the difficulties of experiments. Based on the importance of precipitates in 2xxx series aluminum alloys, the properties mentioned above should be investigated and discussed to reveal the intrinsic behavior of the 2xxx series aluminum alloys. In this paper, we will perform a comprehensive study on these properties of the precipitates using first-principles calculations based on the density functional theory (DFT).

## 2. Model and Computational Method

The crystal structures of precipitates considered in current paper are shown in Figure 1, which include  $\text{Al}_2\text{Cu}$ ,  $\text{Al}_2\text{CuMg}$ ,  $\text{Al}_3\text{Fe}$ ,  $\text{Al}_3\text{Fe}_2\text{Si}$ ,  $\text{Al}_5\text{Cu}_2\text{Mg}_8\text{Si}_6$ ,  $\text{Al}_7\text{Cu}_2\text{Fe}$ ,  $\text{Al}_6\text{Mn}$ ,  $\text{Al}_{20}\text{Cu}_2\text{Mn}_3$ , and  $\text{Al}_3\text{Zr}$ . All these phases are built by their conventional crystal state, and the crystal structures and lattice parameters are shown in Table 1. This work was carried out by using the Cambridge Sequential Total Energy Package (CASTEP) code based on density functional theory (DFT) [13,14]. The criteria for convergence were  $10^{-8}$  eV/atom for total energy, and  $10^{-4}$  eV/Å for Hellmann-Feynman forces, respectively. The Broyden-Fletcher-Goldfarb-Shannon (BFGS) algorithm is applied to optimize the crystal structure including lattice parameters and atomic fractional coordinates. The ultrasoft pseudo-potentials (USPPs) were used to represent the interactions between the ionic core and valence electrons. A plane-wave basis set with  $E_{\text{cut}}$  of 500 eV was used. The exchange and correlation relationship of Perdew-Burke-Ernzerhof (PBE) was applied for calculations [15]. For  $k$ -space, summation the  $0.3 \text{ \AA}^{-1}$  for all phases with Monkhorst-Pack scheme in the first irreducible Brillouin zone [16] has been used. The valence electrons were considered as  $3s^23p^1$ ,  $3d^{10}4s^1$ ,  $2p^63s^2$ ,  $3s^23p^2$ ,  $3d^54s^2$ , and  $4s^24p^64d^25s^2$  for Al, Cu, Mg, Si, Mn, and Zr, respectively. In order to study the mechanical response of the crystals to external stress, the elastic properties are determined using the stress-strain relationship by deforming the unit cell using lagrangian strain modes based on Hooker's law [17].

In order to calculate the thermal expansion coefficient (TEC), the Helmholtz free energy was given by  $F(V, T) = E_{\text{gs}}(V) + F_{\text{vib}}(V, T) + F_{\text{ele}}(V, T)$  [18]. The  $E_{\text{gs}}$  refers to total energy with ground-state obtained directly by DFT calculation at 0 K. The vibrational free energy ( $F_{\text{vib}}$ ) was calculated by means of the quasi-harmonic approximation (QHA) based on the empirical Debye model [19,20].  $F_{\text{ele}}$  is the electron thermal excitations at finite temperature and can be calculated by Mermin statistics  $F_{\text{ele}} = E_{\text{ele}} - TS_{\text{ele}}$ . Using isothermal curves ( $F(V, T) - V$ ), the equilibrium volumes ( $V$ ) at different temperatures can be obtained from the Birch-Murnaghan equation of state (EOS) [21]. Finally, the volumetric TEC  $\lambda(T)$  can be determined by  $\lambda = \frac{1}{V_0} \left( \frac{dV}{dT} \right)$ .

$$E(V) = \frac{B_0 V_0}{B_0'} \left[ \frac{1}{B_0' - 1} \left( \frac{V}{V_0} \right)^{(1-B_0')} + \frac{V}{V_0} + \frac{B_0'}{1 - B_0'} \right] + E_0 \quad (1)$$

where  $E(V)$  is the total energy,  $B_0$ ,  $V_0$ , and  $E_0$  refer to the equilibrium bulk modulus, volume and energy, and  $B_0'$  is the pressure derivation.

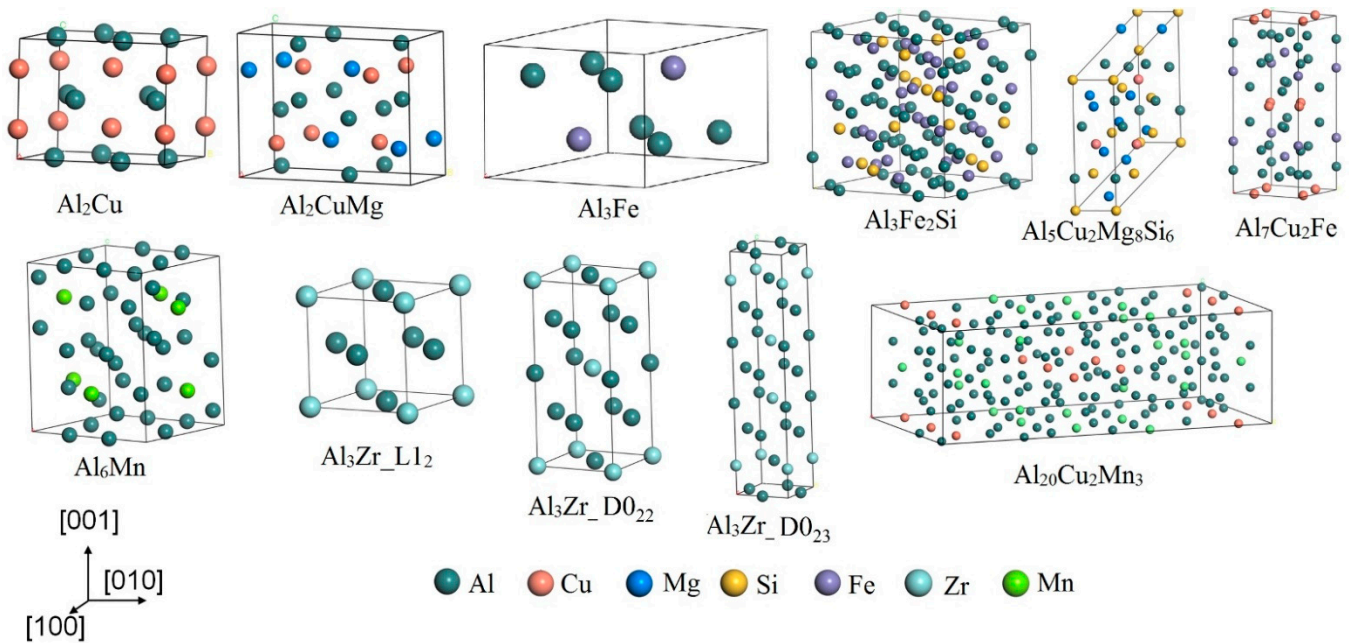


**Figure 1.** The unit crystal cells of second phases in the 2xxx series aluminum alloys.

**Table 1.** Theoretically calculated crystal structure, equilibrium lattice parameters ( $V$  in  $\text{\AA}^3$ ,  $a$ ,  $b$ ,  $c$  in  $\text{\AA}$ ), formation enthalpies (eV/atom) and cohesive energy (eV/atom) of second phases of 2xxx series aluminum alloys.

Phase	Crystal Structure	Space Group	$V$	Crystal Parameters			$\Delta H$	$E_{\text{coh}}$	$D_F$
				$a$	$b$	$c$			
$\text{Al}_2\text{Cu}$	Tetragonal	I4/MCM	179.8 (179.8 <sup>a</sup> )	6.04 (6.039 <sup>a</sup> , 6.063 <sup>b</sup> , 5.99 <sup>c</sup> )	6.04 (6.039 <sup>a</sup> , 6.063 <sup>b</sup> , 5.99 <sup>c</sup> )	4.928 (4.93 <sup>a</sup> , 4.872 <sup>b</sup> , 4.81 <sup>c</sup> )	-0.151 (-0.164 <sup>a</sup> , -0.203 <sup>b</sup> , -0.203 <sup>c</sup> )	-4.0 (-3.89 <sup>a</sup> , -3.99 <sup>b</sup> , -3.99 <sup>c</sup> )	0.19 (0.19 <sup>a</sup> )
$\text{Al}_2\text{CuMg}$	Orthorhombic	CMCM	268.2 (268.1 <sup>a</sup> , 270.8 <sup>d</sup> )	4.027 (4.026 <sup>a</sup> , 4.01 <sup>b</sup> , 3.89 <sup>c</sup> , 4.05 <sup>d</sup> , 4.01 <sup>e</sup> )	9.319 (9.326 <sup>a</sup> , 9.25 <sup>b</sup> , 9.20 <sup>c</sup> , 9.28 <sup>d</sup> , 9.27 <sup>e</sup> )	7.147 (7.142 <sup>a</sup> , 7.15 <sup>b</sup> , 7.16 <sup>c</sup> , 7.21 <sup>d</sup> , 7.12 <sup>e</sup> )	-0.17 (-0.186 <sup>a</sup> , -0.25 <sup>b</sup> , -0.25 <sup>c</sup> )	-3.5 (-3.35 <sup>a</sup> , -3.46 <sup>b</sup> , -3.46 <sup>c</sup> )	0.16 (0.13 <sup>a</sup> )
$\text{Al}_3\text{Fe}$	Triclinic	P63/MMC	108.2 (108.2 <sup>f</sup> )	5.36 (5.357 <sup>f</sup> )	5.36 (5.357 <sup>f</sup> )	4.354 (4.354 <sup>f</sup> )	-0.16 (-0.154 <sup>f</sup> )	-5.3	0.33
$\text{Al}_3\text{Fe}_2\text{Si}$	Cubic	FD-3M	1224.9 (1225 <sup>g</sup> )	10.701	10.701	10.701	-0.423 (-0.402 <sup>f</sup> )	-6.4	0.33
$\text{Al}_5\text{Cu}_2\text{Mg}_8\text{Si}_6$	Monoclinic	PM	385.8	10.479 (10.423 <sup>h</sup> )	4.016 (4.033 <sup>h</sup> )	10.529	-0.02 (-0.12 <sup>h</sup> )	-3.5	0.13
$\text{Al}_7\text{Cu}_2\text{Fe}$	Tetragonal	P4/MNC	590.5	6.324 (6.336 <sup>i</sup> , 6.338 <sup>j</sup> )	6.324 (6.336 <sup>i</sup> , 6.338 <sup>j</sup> )	14.763 (14.87 <sup>i</sup> , 14.83 <sup>j</sup> )	-0.266 (-0.298 <sup>j</sup> )	-4.6	0.14
$\text{Al}_6\text{Mn}$	Orthorhombic	CMCM	431.4	6.468 (6.499 <sup>k</sup> )	7.544 (7.555 <sup>k</sup> )	8.841 (8.872 <sup>k</sup> )	-0.195	-4.7	0.14
$\text{Al}_3\text{Zr}_{\text{D}023}$	Tetragonal	I4/MMM	280.1	4.020 (4.018 <sup>a</sup> , 4.015 <sup>b</sup> )	4.020 (4.018 <sup>a</sup> , 4.015 <sup>b</sup> )	17.332 (17.348 <sup>a</sup> , 17.454 <sup>b</sup> )	-0.489 (-0.517 <sup>a</sup> , -0.459 <sup>b</sup> )	-5.1 (5.14 <sup>a</sup> , 4.57 <sup>b</sup> )	0.15 (0.15 <sup>a</sup> )
$\text{Al}_3\text{Zr}_{\text{D}022}$	Tetragonal	I4/MMM	141.8	3.963	3.963	9.032	-0.464 (-0.463 <sup>l</sup> )	-5.1	0.2
$\text{Al}_3\text{Zr}_{\text{L}12}$	Cubic	PM-3M	69.4	4.109 (4.111 <sup>m</sup> , 4.05 <sup>n</sup> , 4.09 <sup>o</sup> )	4.109 (4.111 <sup>m</sup> )	4.109 (4.111 <sup>m</sup> )	-0.461 (-0.463 <sup>l</sup> , -0.487 <sup>m</sup> , -0.47 <sup>p</sup> )	-5.1	0.18
$\text{Al}_{20}\text{Cu}_2\text{Mn}_3$	Orthorhombic	BBMM	2337.3	24.089 (23.98 <sup>q</sup> )	12.601 (12.54 <sup>q</sup> )	7.700 (7.66 <sup>q</sup> )	-0.181 (-0.156 <sup>q</sup> )	-4.64	0.19

$a$ ,  $c$ ,  $d$ ,  $f$ ,  $h$ ,  $j$ ,  $m$ ,  $p$ , and  $q$  are the theoretical data from Refs. [22–29], and [9], respectively.  $b$ ,  $e$ ,  $i$ ,  $l$ ,  $n$ , and  $o$  are the experimental data from Refs. [30–35], respectively. <sup>g</sup> The Inorganic Crystal Structure Database (ICSD ID: 422341). <sup>k</sup> Exp. data from Refs. [36,37].

### 3. Results and Discussion

#### 3.1. Mechanical Properties

Table 1 listed the equilibrium lattice parameters, formation enthalpies and cohesive energy of precipitates in 2xxx series aluminum alloys. The optimized lattice parameters are in good agreement with the references. The thermodynamic stability usually requires

the formation enthalpy and cohesive energy to be negative. This work provides the calculated formation enthalpies of  $-0.151$ ,  $-0.17$ ,  $-0.16$ ,  $-0.463$ ,  $-0.02$ ,  $-0.266$ ,  $-0.195$ ,  $-0.489$ ,  $-0.464$ ,  $-0.461$ , and  $-0.181$  eV/atom for  $\text{Al}_2\text{Cu}$ ,  $\text{Al}_2\text{CuMg}$ ,  $\text{Al}_3\text{Fe}$ ,  $\text{Al}_3\text{Fe}_2\text{Si}$ ,  $\text{Al}_5\text{Cu}_2\text{Mg}_8\text{Si}_6$ ,  $\text{Al}_7\text{Cu}_2\text{Fe}$ ,  $\text{Al}_6\text{Mn}$ ,  $\text{Al}_3\text{Zr\_D0}_{23}$ ,  $\text{Al}_3\text{Zr\_D0}_{22}$ ,  $\text{Al}_3\text{Zr\_L1}_2$ , and  $\text{Al}_{20}\text{Cu}_2\text{Mn}_3$ , respectively. Therefore, the most thermodynamically stable structure refers to  $\text{Al}_3\text{Zr}$  phase regardless of its polymorphs, while  $\text{Al}_5\text{Cu}_2\text{Mg}_8\text{Si}_6$  behaves the value of  $-0.02$  eV (close to zero) indicating its metastable nature, which may decompose after high-temperature artificial aging.

The second order elastic constants were calculated and listed in Table 2, and the corresponding polycrystalline bulk and shear moduli are given in Table 3 calculated by Reuss and Voigt methods [38], respectively; the real polycrystalline values are estimated by Hill's average [39]. For  $\text{Al}_2\text{Cu}$  and  $\text{Al}_2\text{CuMg}$ ,  $C_{11}$ ,  $C_{22}$ , and  $C_{33}$  are over 100 GPa, which are much higher than other elastic constants, indicating their strong anti-compressibility along principal axes. Especially,  $\text{Al}_2\text{Cu}$  shows the same stiffness along the  $a$ - and  $b$ - axes, both of which are weaker than that along the  $c$ - axis, while  $\text{Al}_2\text{CuMg}$  is stiffer along the  $b$ - axis compared with the  $a$ - or  $c$ - axis. The tabulated elastic modulus ( $C_{44}$ ) of both  $\text{Al}_2\text{Cu}$  and  $\text{Al}_2\text{CuMg}$  is significantly small. This corresponds to the shear mode and indicates their relatively small shear modulus ( $\sim 43$  GPa as shown in Table 3).  $\text{Al}_3\text{Fe}$ ,  $\text{Al}_3\text{Fe}_2\text{Si}$ , and  $\text{Al}_7\text{Cu}_2\text{Fe}$  show much higher elastic constants of  $C_{11}$ ,  $C_{22}$ , and  $C_{33}$  (over 200 GPa), implying these phases are very hard to be deformed.  $\text{Al}_5\text{Cu}_2\text{Mg}_8\text{Si}_6$  is an exception; all elastic constants are much smaller than others, implying its soft nature. Actually,  $\text{Al}_5\text{Cu}_2\text{Mg}_8\text{Si}_6$  is a mechanically unstable phase since it disobeys the well-known Born-Huang stability criterion [40,41]. For Mn-based phases  $\text{Al}_6\text{Mn}$  and  $\text{Al}_{20}\text{Cu}_2\text{Mn}_3$ ,  $\text{Al}_6\text{Mn}$  shows better anti-compressibility along the principal axis than  $\text{Al}_{20}\text{Cu}_2\text{Mn}_3$ , while the shear or complex mode corresponding to  $C_{44}$  or  $C_{12}$  and  $C_{23}$  of  $\text{Al}_6\text{Mn}$  are much smaller than that of  $\text{Al}_{20}\text{Cu}_2\text{Mn}_3$ .  $\text{Al}_3\text{Zr}$  usually has three kinds of polymorphs; the calculated results of both  $\text{D0}_{22}$  and  $\text{L1}_2$  phases are very similar to other references as listed in Table 1, while for the  $\text{D0}_{23}$  phase, the reference calculation results are dispersed from 201 to 284 GPa by taking  $C_{11}$  as an example [42]. To our knowledge, most precipitates of the 2xxx series aluminum alloys have not any experimental values, our study may provide valuable data especially for  $\text{Al}_3\text{Fe}_2\text{Si}$ ,  $\text{Al}_6\text{Mn}$ , etc.

**Table 2.** Theoretically calculated elastic constants ( $C_{ij}$  in GPa) for second phases of 2xxx series aluminum alloys.

Phase	$C_{11}$	$C_{12}$	$C_{13}$	$C_{22}$	$C_{23}$	$C_{33}$	$C_{44}$	$C_{66}$
$\text{Al}_2\text{Cu}$	150.2 (150.3 <sup>a</sup> , 179.7 <sup>b</sup> , 163.8 <sup>c</sup> )	97.4 (86.1 <sup>a</sup> , 72.7 <sup>b</sup> , 78.2 <sup>c</sup> )	59.1 (62.6 <sup>a</sup> , 75.7 <sup>b</sup> , 14.7 <sup>c</sup> )	-	-	211.3 (171.7 <sup>a</sup> , 170.2 <sup>b</sup> , 246.7 <sup>c</sup> )	34.5 (29.4 <sup>a</sup> , 28.0 <sup>b</sup> , 33.8 <sup>c</sup> )	41.3 (45.5 <sup>a</sup> , 44.7 <sup>b</sup> , 37.3 <sup>c</sup> )
$\text{Al}_2\text{CuMg}$	124.7 (156.4 <sup>c</sup> , 115.9 <sup>d</sup> , 133.6 <sup>e</sup> )	22.5 (33.4 <sup>c</sup> , 35.3 <sup>d</sup> , 42.1 <sup>e</sup> )	66.5 (62.6 <sup>c</sup> , 46.8 <sup>d</sup> , 49.9 <sup>e</sup> )	150.5 (175.9 <sup>c</sup> , 174.1 <sup>d</sup> , 138.8 <sup>e</sup> )	40.4 (17.7 <sup>c</sup> , 38.7 <sup>d</sup> , 58.0 <sup>e</sup> )	126.6 (168.8 <sup>c</sup> , 153.1 <sup>d</sup> , 145.2 <sup>e</sup> )	41.2 (43.7 <sup>c</sup> , 50.9 <sup>d</sup> , 39.0 <sup>e</sup> )	32.6 (50.7 <sup>c</sup> , 26.6 <sup>d</sup> , 37.7 <sup>e</sup> )
$\text{Al}_3\text{Fe}$	213.2 (211 <sup>f</sup> )	100.0 (93 <sup>f</sup> )	76.7 (73 <sup>f</sup> )	-	-	228.8 (228 <sup>f</sup> )	41.3 (39 <sup>f</sup> )	57.4 (59 <sup>f</sup> )
$\text{Al}_3\text{Fe}_2\text{Si}$	288.2	89.8	-	-	-	93.2	-	-
$\text{Al}_5\text{Cu}_2\text{Mg}_8\text{Si}_6$	126.8 (146.3 <sup>g</sup> )	39.7 (42.8 <sup>g</sup> )	30.8 (33.3 <sup>g</sup> )	-	-	126.3 (123.3 <sup>g</sup> )	<0	<0
$\text{Al}_7\text{Cu}_2\text{Fe}$	225.0 (206 <sup>h</sup> )	50.7 (50.6 <sup>h</sup> )	52.6 (65.7 <sup>h</sup> )	-	-	217.8 (194 <sup>h</sup> )	99.5 (80.9 <sup>h</sup> )	86.5 (71.1 <sup>h</sup> )
$\text{Al}_6\text{Mn}$	200.3	36.0	71.3	229.7	51.6	171.4	48.1	67.4
$\text{Al}_3\text{Zr\_D0}_{23}$	203.4 (284.3 <sup>i</sup> , 206.7 <sup>j</sup> , 201.3 <sup>k</sup> )	65.6 (67.8 <sup>i</sup> , 52.3 <sup>j</sup> , 70.5 <sup>k</sup> )	43.1 (58.8 <sup>i</sup> , 50.7 <sup>j</sup> , 49.1 <sup>k</sup> )	-	-	204.0 (175.9 <sup>i</sup> , 182.6 <sup>j</sup> , 196.7 <sup>k</sup> )	83.0 (79.2 <sup>i</sup> , 81.4 <sup>j</sup> , 80.8 <sup>k</sup> )	101.4 (97.2 <sup>i</sup> , 75.9 <sup>j</sup> )
$\text{Al}_3\text{Zr\_D0}_{22}$	183.2 (185.96 <sup>l</sup> )	87.4 (85.34 <sup>l</sup> )	42.0 (43.13 <sup>l</sup> )	-	-	203.7 (202.08 <sup>l</sup> )	89.0 (90 <sup>l</sup> )	126.0 (125.22 <sup>l</sup> )
$\text{Al}_3\text{Zr\_L1}_2$	173.6 (182.8 <sup>m</sup> , 179 <sup>n</sup> )	65.4 (65.2 <sup>m</sup> , 66 <sup>n</sup> )	-	-	-	-	69.2 (70.1 <sup>m</sup> , 69 <sup>n</sup> )	-
$\text{Al}_{20}\text{Cu}_2\text{Mn}_3$	138.0	69.6	81.0	177.5	73.0	150.4	24.6	46.8

a, c, d, e, f, g, h, i, j, k, l, m, and n are the theoretical data from Refs. [22–28,42–44], and [45], respectively. <sup>b</sup> Exp. Data from Ref. [46].

Based on the values of the Voigt-Reuss-Hill approximation shown in Table 2, the Young's modulus and Poisson's ratio can be calculated by  $E = 9BG/(3B + G)$  and  $\sigma = (3B - 2G)/(6B + 2G)$ , respectively. Generally, the mechanical moduli of precipitates of 2xxx series aluminum alloys are similar to previously reported values. As shown in Figure 2, the variation trend of bulk, shear, and Young's moduli shares a similar tendency, in which  $\text{Al}_3\text{Fe}_2\text{Si}$  behaves the highest values. Bulk modulus, for instance, which is derived from 63.5 to 155.9 GPa, has the trend of:  $\text{Al}_3\text{Fe}_2\text{Si} > \text{Al}_3\text{Fe} > \text{Al}_7\text{Cu}_2\text{Fe} > \text{Al}_6\text{Mn} \approx \text{Al}_3\text{Zr} \approx \text{Al}_{20}\text{Cu}_2\text{Mn}_3 > \text{Al}_2\text{Cu} > \text{Al}_2\text{CuMg} > \text{Al}_5\text{Cu}_2\text{Mg}_8\text{Si}_6$ . All iron-based compounds of

Al<sub>3</sub>Fe<sub>2</sub>Si, Al<sub>3</sub>Fe, and Al<sub>7</sub>Cu<sub>2</sub>Fe have a large bulk modulus, which is more or less smaller than BCC-iron (~174 GPa [47]). Young's modulus usually reflects the plastic deformation ability of bulk materials; this work proves the ultrahigh anti-deformation nature of Al<sub>7</sub>Cu<sub>2</sub>Fe. For three polymorphs of Al<sub>3</sub>Zr, the Young's modulus of D0<sub>23</sub> and D0<sub>22</sub> phases are similar (~196 GPa), which are much higher than the L1<sub>2</sub> phase (~156 GPa), indicating their outstanding mechanical behavior. Typically, for covalent and ionic materials, the value of Poisson's ratio is 0.1 and 0.25, respectively, whereas for metallic materials, the value is 0.3 [48]. Most of second phases have the Poisson's ratio of ~0.3, such as Al<sub>2</sub>Cu, Al<sub>3</sub>Fe, Al<sub>5</sub>Cu<sub>2</sub>Mg<sub>8</sub>Si<sub>6</sub>, and Al<sub>20</sub>Cu<sub>2</sub>Mn<sub>3</sub>, indicating their advanced metallic nature. For Al<sub>2</sub>CuMg, Al<sub>3</sub>Fe<sub>2</sub>Si, Al<sub>6</sub>Mn, and Al<sub>3</sub>Zr, they are dominated by a mainly covalent bond. The brittle index of *B/G* is applied to analyze the ductility of phases. The higher the value of *B/G*, the better the ductility of the materials. The present work indicates that Al<sub>2</sub>Cu, Al<sub>3</sub>Fe, Al<sub>5</sub>Cu<sub>2</sub>Mg<sub>8</sub>Si<sub>6</sub>, and Al<sub>20</sub>Cu<sub>2</sub>Mn<sub>3</sub> are ductile phases, which are in agreement with their advanced metallic nature. For the three Al<sub>3</sub>Zr polymorphs, the L1<sub>2</sub> phase shows the best ductility. Furthermore, in the present work, a semi-empirical model proposed by Chen et al. [49] was employed to evaluate the Vicker's hardness. As shown in Table 3, the hardness of Al<sub>3</sub>Zr\_ D0<sub>22</sub> and D0<sub>23</sub> phases is very high (~18GPa), which is comparable to the value of Al<sub>7</sub>Cu<sub>2</sub>Fe; whereas Al<sub>5</sub>Cu<sub>2</sub>Mg<sub>8</sub>Si<sub>6</sub> is quite soft since its hardness is only 2.7 GPa. The common precipitates of Al<sub>2</sub>Cu and Al<sub>2</sub>CuMg show a moderate hardness of 4.3 GPa and 6.8 GPa, which are much softer than Al<sub>6</sub>Mn or Al<sub>3</sub>Zr phases.

**Table 3.** Theoretically calculated elastic properties including bulk modulus (*B* in GPa) and its pressure derivative (*B'*), shear modulus (*G* in GPa), Young's modulus (*E* in GPa), Poisson ratio (*σ*), and anisotropy factors (*A<sub>B</sub>*, *A<sub>C</sub>* and *A<sup>U</sup>*) for second phases of 2xxx series aluminum alloys.

Phase	<i>B</i>			<i>B'</i>	<i>G</i>			<i>B<sub>H</sub>/G<sub>H</sub></i>	<i>E</i>	<i>σ</i>	<i>Hv</i>	<i>A<sub>B</sub></i>	<i>A<sub>C</sub></i>	<i>A<sup>U</sup></i>
	<i>B<sub>V</sub></i>	<i>B<sub>R</sub></i>	<i>B<sub>H</sub></i>		<i>G<sub>V</sub></i>	<i>G<sub>R</sub></i>	<i>G<sub>H</sub></i>							
Al <sub>2</sub> Cu	90.5 (99.4 <sup>a</sup> , 87.7 <sup>b</sup> )	90.5 (99.4 <sup>a</sup> , 87.6 <sup>b</sup> )	90.5 (99.4 <sup>a</sup> , 87.7 <sup>b</sup> , 108.6 <sup>c</sup> )	4.71	46.1 (38.3 <sup>a</sup> , 52.1 <sup>b</sup> )	38.2 (35.9 <sup>a</sup> , 42.3 <sup>b</sup> )	42.1 (37.1 <sup>a</sup> , 47.2 <sup>b</sup> , 39 <sup>c</sup> )	2.1	109.5 (99 <sup>a</sup> , 120 <sup>b</sup> , 104.5 <sup>c</sup> )	0.298 (0.33 <sup>a</sup> , 0.272 <sup>b</sup> , 0.34 <sup>c</sup> )	4.3	0	0.09	1.03
Al <sub>2</sub> CuMg	73.4 (80.9 <sup>b</sup> , 76.06 <sup>d</sup> )	72.9 (80.7 <sup>b</sup> , 74.36 <sup>d</sup> )	73.2 (80.8 <sup>b</sup> , 75.21 <sup>d</sup> , 79.48 <sup>e</sup> )	4.639	45.6 (63.3 <sup>b</sup> , 51.02 <sup>d</sup> )	41.1 (57.9 <sup>b</sup> , 45.13 <sup>d</sup> )	43.3 (60.6 <sup>b</sup> , 48.08 <sup>d</sup> , 46.8 <sup>e</sup> )	1.7 (1.564 <sup>d</sup> )	108.5 (145.5 <sup>b</sup> , 118.9 <sup>d</sup> , 117.3 <sup>e</sup> )	0.253 (0.2 <sup>b</sup> , 0.237 <sup>d</sup> , 0.254 <sup>e</sup> )	6.8	0.003	0.052	0.554 (0.675 <sup>d</sup> , 0.349 <sup>e</sup> )
Al <sub>3</sub> Fe	129.6 (125 <sup>f</sup> )	129.5 (125 <sup>f</sup> )	129.6 (125 <sup>f</sup> )	4.156	54.9 (55 <sup>f</sup> )	52.0 (51 <sup>f</sup> )	53.4 (53 <sup>f</sup> )	2.4	140.9	0.319 (0.31 <sup>f</sup> )	4.3	0.0003	0.027	0.281 (0.35 <sup>f</sup> )
Al <sub>3</sub> Fe <sub>2</sub> Si	155.9	155.9	155.9	4.498	95.6	95.5	95.6	1.6	238.1	0.245	13.3	0	0.0005	0.0052
Al <sub>5</sub> Cu <sub>2</sub> Mg <sub>8</sub> Si <sub>6</sub>	63.6 (70.5 <sup>g</sup> )	63.4 (69.7 <sup>g</sup> )	63.5 (70.1 <sup>g</sup> )	4.439	5.8 (44.5 <sup>g</sup> )	51.8 (42.8 <sup>g</sup> )	28.8 (43.6 <sup>g</sup> )	2.2	75.0 (108.4 <sup>g</sup> )	0.303 (0.242 <sup>g</sup> )	2.7	/	/	/
Al <sub>7</sub> Cu <sub>2</sub> Fe	109.1	109.0	109.1 (107.8 <sup>h</sup> )	4.42	91.3	90.8	91.0 (74.5 <sup>h</sup> )	1.2	213.6 (181.7 <sup>h</sup> )	0.173 (0.219 <sup>h</sup> )	19.6	0.0005	0.0027	0.0285
Al <sub>6</sub> Mn	102.1	101.9	102.0 (102.6 <sup>i</sup> )	4.022	67.6	64.1	65.9	1.5	126.6	0.234	10.9	0.001	0.0266	0.275
Al <sub>3</sub> Zr_D0 <sub>23</sub>	101.6 (123.9 <sup>j</sup> )	101.4 (117.4 <sup>j</sup> )	101.5 (120.6 <sup>j</sup> , 100.2 <sup>k</sup> )	3.977	84.1 (88.4 <sup>j</sup> )	82.8 (85.8 <sup>j</sup> )	83.4 (87.1 <sup>j</sup> , 77.1 <sup>k</sup> )	1.2	196.2 (210.6 <sup>j</sup> , 184.1 <sup>k</sup> )	0.177 (0.195 <sup>k</sup> )	18.1	0.001	0.008	0.081
Al <sub>3</sub> Zr_D0 <sub>22</sub>	101.4 (101.9 <sup>l</sup> )	101.2 (101.6 <sup>l</sup> )	101.3 (101.8 <sup>l</sup> )	3.11	87.4 (87.9 <sup>l</sup> )	79.3 (80.6 <sup>l</sup> )	83.3 (84.2 <sup>l</sup> )	1.2	196.2 (198 <sup>l</sup> )	0.177 (0.176 <sup>l</sup> )	18.1	0.001	0.0486	0.513
Al <sub>3</sub> Zr_L1 <sub>2</sub>	101.5	101.5	101.5 (104.4 <sup>m</sup> , 103 <sup>n</sup> )	4.134	63.1	62.2	62.7 (65.3 <sup>m</sup> , 64 <sup>n</sup> )	1.6	156.0 (162.2 <sup>m</sup> , 159.1 <sup>n</sup> )	0.244 (0.241 <sup>m</sup> , 0.243 <sup>n</sup> )	9.8	0	0.0072	0.0723
Al <sub>20</sub> Cu <sub>2</sub> Mn <sub>3</sub>	101.5	100.8	101.1	4.741	42.5	38.2	40.4	2.5	106.9	0.324	3.0	0.0035	0.0533	0.569

a, b, c, d, e, f, g, h, i, j, k, l, m, and n are the theoretical data from Refs. [22–28,43,44,50–52], and [45], respectively.

The mechanical anisotropy of crystals is also characterized by using 3-D mechanical modulus and anisotropy indexes. Firstly, the directional dependence of the Young's modulus for different crystals can be evaluated by [53]:

For tetragonal (Al<sub>2</sub>Cu, Al<sub>7</sub>Cu<sub>2</sub>Fe, Al<sub>3</sub>Zr\_D0<sub>23</sub> and D0<sub>22</sub>):

$$E = \left[ (l_1^4 + l_2^4) s_{11} + l_3^4 s_{33} + l_1^2 l_2^2 (2s_{12} + s_{66}) + l_3^2 (1 - l_3^2) (2s_{13} + s_{44}) \right]^{-1} \quad (2)$$

For orthorhombic (Al<sub>2</sub>CuMg, Al<sub>6</sub>Mn, Al<sub>20</sub>Cu<sub>2</sub>Mn<sub>3</sub>):

$$E = \left[ l_1^4 s_{11} + l_2^4 s_{22} + l_3^4 s_{33} + 2l_1^2 l_2^2 s_{12} + 2l_1^2 l_3^2 s_{13} + 2l_2^2 l_3^2 s_{23} + l_1^2 l_2^2 s_{66} + l_1^2 l_3^2 s_{55} + l_2^2 l_3^2 s_{44} \right]^{-1} \quad (3)$$

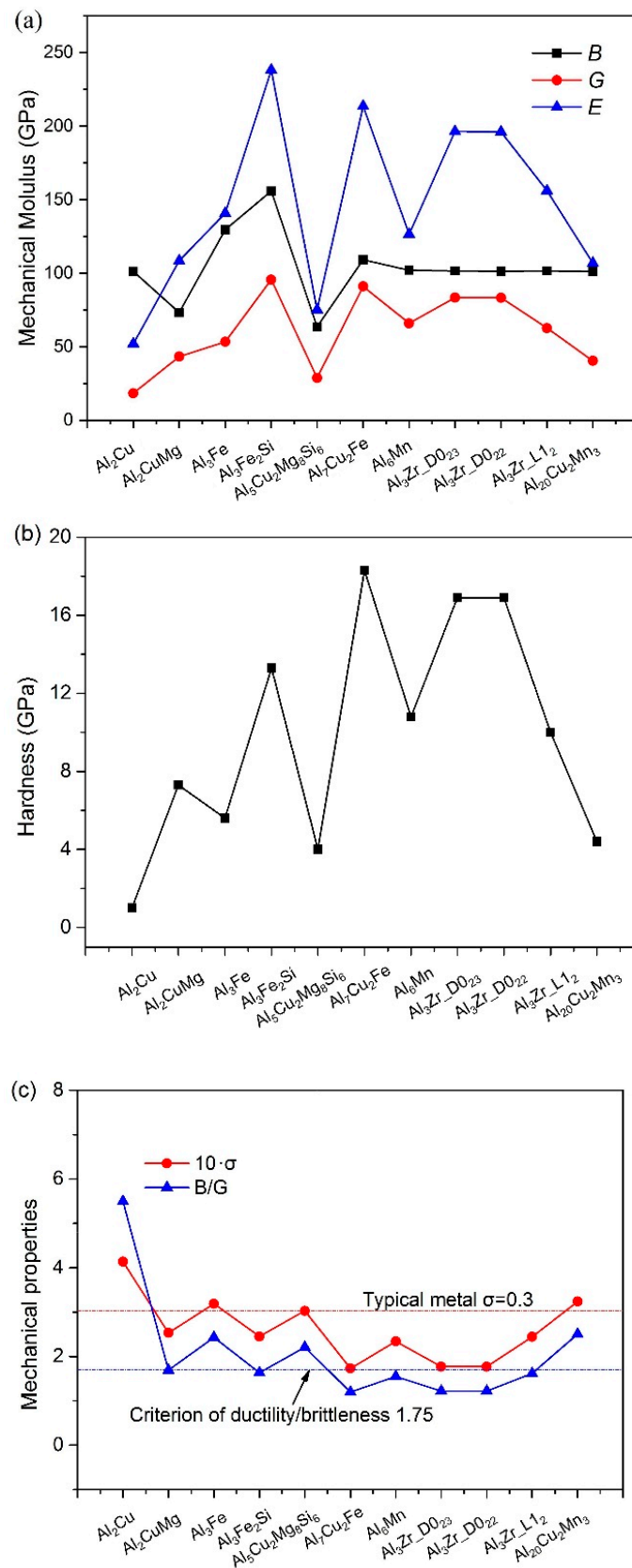


**Figure 2.** Mechanical properties of second phases in the 2xxx series aluminum alloys: (a) bulk, shear, and Young’s moduli, (b) Vicker’s hardness, and (c) Poisson’s ratio, and brittle index; the horizontal lines refer to the typical Poisson’s ratio value (~0.3) for pure metal, and criterion of ductility/brittleness ( $B/G = 1.75$ ).

For triclinic ( $\text{Al}_3\text{Fe}$ ):

$$E = \left[ \begin{aligned} & l_1^4 s_{11} + 2l_1^2 l_2^2 s_{12} + 2l_1^2 l_3^2 s_{13} + 2l_1^2 l_2 l_3 s_{14} + 2l_1^3 l_3 s_{15} + 2l_1^3 l_2 s_{16} + l_2^4 s_{22} + 2l_2^2 l_3^2 s_{23} \\ & + 2l_2^3 l_3 s_{24} + 2l_1 l_2^2 l_3 s_{25} + 2l_1 l_2^3 s_{26} + l_3^4 s_{33} + 2l_2 l_3^3 s_{34} + 2l_1 l_3^3 s_{35} + 2l_1 l_2 l_3^2 s_{36} \\ & + l_2^2 l_3^2 s_{44} + 2l_1 l_2 l_3^2 s_{45} + 2l_1 l_2^2 l_3 s_{46} + l_1^2 l_3^2 s_{55} + 2l_1^2 l_2 l_3 s_{56} + l_1^2 l_2^2 s_{66} \end{aligned} \right]^{-1} \quad (4)$$

For cubic ( $\text{Al}_3\text{Fe}_2\text{Si}$ ,  $\text{Al}_3\text{Zr\_L1}_2$ ):

$$E = \left[ s_{11} - 2 \left( s_{11} - s_{12} - \frac{1}{2} s_{44} \right) \left( l_1^2 l_2^2 + l_2^2 l_3^2 + l_3^2 l_1^2 \right) \right]^{-1} \quad (5)$$

For monoclinic ( $\text{Al}_5\text{Cu}_2\text{Mg}_8\text{Si}_6$ ):

$$E = \left[ \begin{aligned} & l_1^4 s_{11} + 2l_1^2 l_2^2 s_{12} + 2l_1^2 l_3^2 s_{13} + 2l_1^3 l_3 s_{15} + l_2^4 s_{22} + 2l_2^2 l_3^2 s_{23} + 2l_1 l_2^2 l_3 s_{25} \\ & + l_3^4 s_{33} + 2l_1 l_3^3 s_{35} + l_2^2 l_3^2 s_{44} + 2l_1 l_2^2 l_3 s_{46} + l_1^2 l_3^2 s_{55} + l_1^2 l_2^2 s_{66} \end{aligned} \right]^{-1} \quad (6)$$

In the above equations,  $l_1 = \sin \theta \cos \varphi$ ,  $l_2 = \sin \theta \sin \varphi$ , and  $l_3 = \cos \theta$ . The results are shown in Figure 3.  $\text{Al}_2\text{Cu}$  and  $\text{Al}_5\text{Cu}_2\text{Mg}_8\text{Si}_6$  show significantly stronger anisotropy than other phases, since the surface contours show a large deviation from the perfect spherical shape, while the iron-based compounds  $\text{Al}_3\text{Fe}_2\text{Si}$  and  $\text{Al}_7\text{Cu}_2\text{Fe}$  are very isotropy. As for the three  $\text{Al}_3\text{Zr}$  phases, the  $\text{L1}_2$  structure shows the best isotropic nature. More direct information can be seen from the planar projections on the (001) and (110) crystal planes in Figure 4. On the (001) plane,  $\text{Al}_2\text{CrMg}$  shows the strongest anisotropy character, while on the (110) plane,  $\text{Al}_5\text{Cu}_2\text{Mg}_8\text{Si}_6$  has the extremely strong anisotropy as can be seen from the green line in Figure 4b.

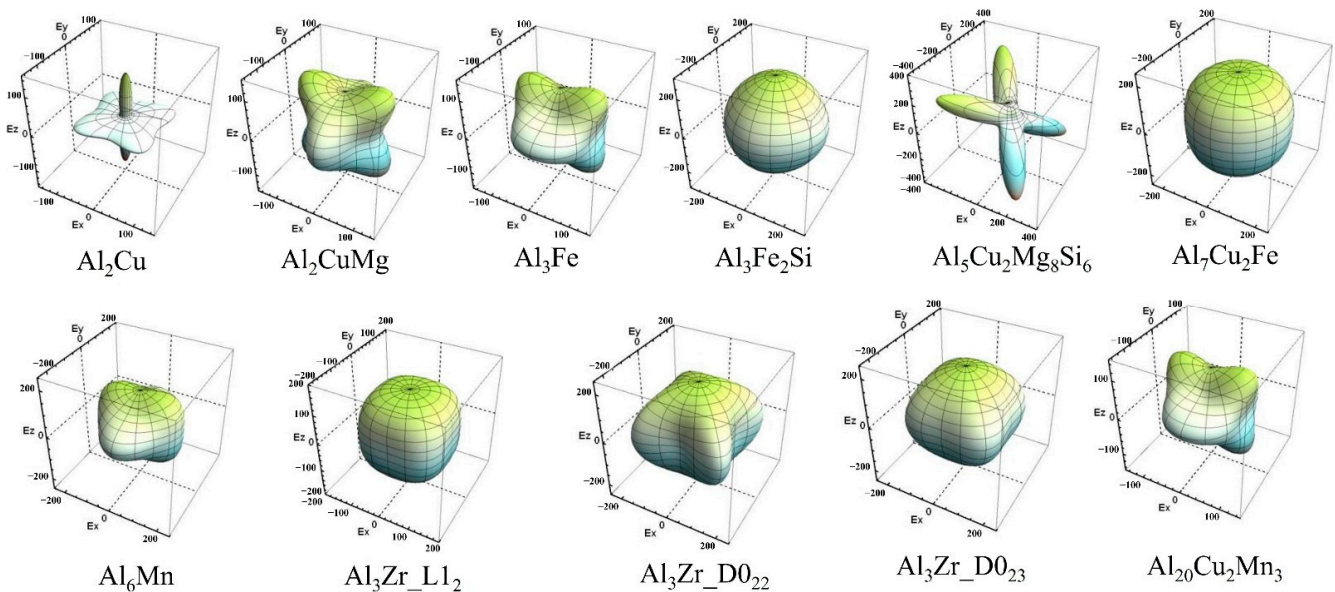


**Figure 3.** The surface constructions of the Young's modulus of second phases in the 2xxx series aluminum alloys.

Three commonly used anisotropy indexes ( $A_B$ ,  $A_G$  and  $A^U$ ) were calculated and shown in Table 3, where  $A_B = (B_V - B_R)/(B_V + B_R)$ ,  $A_G = (G_V - G_R)/(G_V + G_R)$ , and  $A^U = 5(G_V/G_R) + (B_V/B_R) - 6$ . For  $\text{Al}_2\text{Cu}$  and  $\text{Al}_2\text{CuMg}$  [54], the calculated  $A_B$  of  $\text{Al}_2\text{Cu}$  is zero, which indicates the perfect isotropy of  $\text{Al}_2\text{Cu}$  in compression, while  $\text{Al}_2\text{CuMg}$  has a high value of  $A_B$  indicating its anisotropic nature. As for shear mode,  $\text{Al}_2\text{Cu}$  has a high value of  $A_G$ , implying its anisotropic character. The universal anisotropy index of  $A^U$  follows the trend of:  $\text{Al}_2\text{Cu} > \text{Al}_2\text{CuMg} \approx \text{Al}_3\text{Zr\_D0}_{22} \approx \text{Al}_{20}\text{Cu}_2\text{Mn}_3 > \text{Al}_3\text{Fe} \approx \text{Al}_6\text{Mn} > \text{Al}_3\text{Zr\_D0}_{23} \approx \text{Al}_3\text{Zr\_L1}_2 > \text{Al}_7\text{Cu}_2\text{Fe} > \text{Al}_3\text{Fe}_2\text{Si}$ .

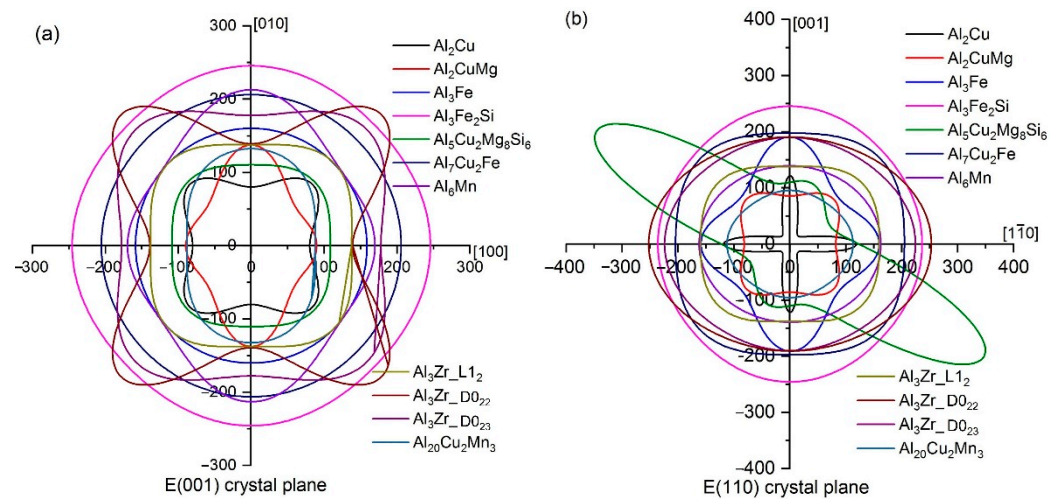


**Figure 4.** The planar projections of the Young's modulus of second phases in the 2xxx series aluminum alloys: (a) (001) crystal plane, and (b) (110) crystal plane.

### 3.2. Thermophysical Properties

The precipitation influences thermophysical properties such as thermoelectric power, the thermal expansion coefficient, and thermal conductivity. In this part, the sound velocity and the Debye temperature were calculated. The longitudinal, transverse, and average wave velocities are given by [55]:

$$v_m = \left[ \frac{1}{3} \left( \frac{2}{v_t^3} + \frac{1}{v_l^3} \right) \right]^{-1/3} \quad (7)$$

$$v_l = \sqrt{\left( B + \frac{4}{3}G \right) \frac{1}{\rho}} \quad (8)$$

Then, the Debye temperature is given by [56]:

$$\Theta_D = \frac{h}{k_B} \left[ \frac{3n}{4\pi} \left( \frac{N_A \rho}{M} \right) \right]^{1/3} v_m \quad (9)$$

where  $\Theta_D$  is the Debye temperature, and  $h$ ,  $k_B$  and  $N_A$  are the Planck, Boltzmann and Avogadro constants, respectively;  $n$  is atomic number;  $M$  is molecular weight, and  $\rho$  is volumetric density;  $v_l$ ,  $v_t$  and  $v_m$  are longitudinal, transverse, and average acoustic velocities, respectively. The results are shown in Table 4, the sound velocity of  $\text{Al}_3\text{Fe}_2\text{Si}$  is highest among all considered phases, since it behaves the greatest mechanical moduli and small density, and therefore, the Debye temperature of  $\text{Al}_3\text{Fe}_2\text{Si}$  is as high as 622 K. The Debye temperatures obey the trend of:  $\text{Al}_3\text{Fe}_2\text{Si} > \text{Al}_3\text{Zr\_D0}_{23} > \text{Al}_6\text{Mn} > \text{Al}_3\text{Zr\_D0}_{22} > \text{Al}_7\text{Cu}_2\text{Fe} > \text{Al}_3\text{Fe} > \text{Al}_2\text{CuMg} > \text{Al}_{20}\text{Cu}_2\text{Mn}_3 > \text{Al}_2\text{Cu} > \text{Al}_3\text{Zr\_L1}_2$ .

The thermal expansion is an important thermophysical character, which characterizes the anharmonicity of crystals. At different temperatures, the Helmholtz free energy of  $\text{Al}_2\text{Cu}$  is shown in Figure 5a, based on which the volume expansion ( $\Delta V/V_0$ ) and bulk modulus can be fitted by the well-known Birch-Murnaghan's equation of states (EOS) [57]. Figure 5b shows the volume' expansions ( $\Delta V/V_0$ ) versus temperature curve by taking  $\text{Al}_2\text{Cu}$  as an example. Then, the linear thermal expansion coefficient (LTEC) is obtained and plotted in Figure 6. For the  $\text{Al}_2\text{Cu}$  phase, the LTEC along the  $a$  or  $c$  axis is also calculated, which implies that the value of  $\alpha_c$  is much higher than that of  $\alpha_a$ . The calculated average LTEC is  $\sim 16.2 \text{ ppm K}^{-1}$  from 300 to 800 K, which is similar to the experimental data ( $\sim 17.2 \text{ ppm K}^{-1}$ ) [33]. For  $\text{Al}_3\text{Zr}$  polymorphs, the results are plotted in Figure 6b, and our results indicate that the  $\text{L1}_2$  phase has the highest LTEC value, followed by  $\text{D0}_{23}$ , and the lowest one refers to  $\text{D0}_{22}$ . From 300 K to 800 K, our calculated values are in extreme agreement with the calculated data given by Saha et al. [58], although both of our curves

are slightly higher than experimental curve [59], as shown in Figure 6b. The calculated LTEC of three Al<sub>3</sub>Zr polymorphs follow the order of L<sub>12</sub> > D<sub>023</sub> > D<sub>022</sub>; all of them show a much lower value than pure Al substance. Overall, all calculated average LTECs are given in Figure 6c; in this figure the pure Al substance is also plotted. Al<sub>2</sub>CuMg shows the highest LTEC, followed by Al<sub>3</sub>Fe, Al<sub>2</sub>Cu, Al<sub>3</sub>Zr\_L<sub>12</sub> and others, while Al<sub>3</sub>Zr\_D<sub>022</sub> is the lowest one; the discrepancy between *a*-Al and Al<sub>2</sub>CuMg is the smallest, which may decrease the heat misfit degree between them and improve the thermal shock resistant property, and thereby delay the initiation and propagation of thermal crack at the interface.

**Table 4.** Calculated sound velocities (km/s) of second phases of 2xxx series aluminum alloys; the Debye temperatures (K) are also shown below.

Phase	$v_l$	$v_t$	$v_m$	$\Theta_D$
Al <sub>2</sub> Cu	5.812	3.114	3.478	420
Al <sub>2</sub> CuMg	6.105	3.512	3.9	438
Al <sub>3</sub> Fe	6.992	3.622	4.055	484
Al <sub>3</sub> Fe <sub>2</sub> Si	7.7	4.499	4.989	622
Al <sub>7</sub> Cu <sub>2</sub> Fe	6.863	4.02	4.458	532
Al <sub>6</sub> Mn	7.637	4.553	5.041	557
Al <sub>3</sub> Zr_D <sub>023</sub>	7.184	4.484	4.94	584
Al <sub>3</sub> Zr_D <sub>022</sub>	7.017	4.258	4.705	554
Al <sub>3</sub> Zr_L <sub>12</sub>	6.128	3.105	3.48	387
Al <sub>20</sub> Cu <sub>2</sub> Mn <sub>3</sub>	6.472	3.303	3.701	424

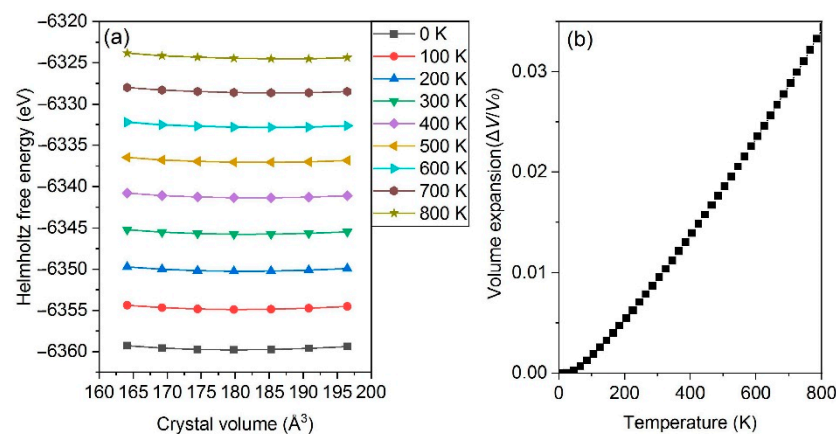


**Figure 5.** Dependence of the Helmholtz free energy,  $F(V, T)$ , on the crystal volume under different temperatures (a) by taking Al<sub>2</sub>Cu for example, based on which the volume' expansions ( $\Delta V/V_0$ ) are given in (b).

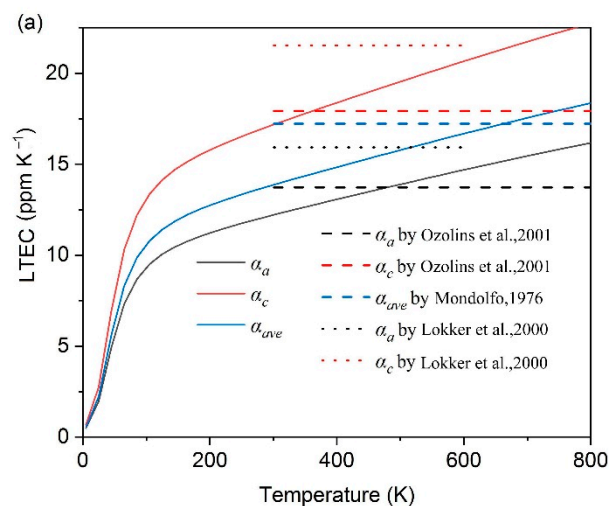


**Figure 6.** Cont.

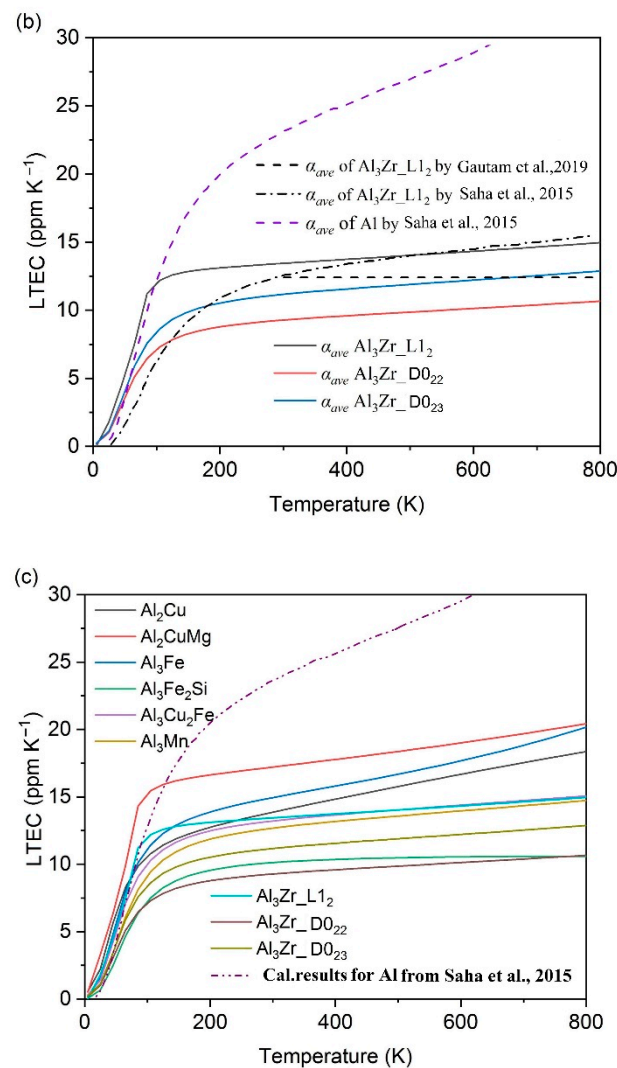


**Figure 6.** Linear thermal expansion coefficients (LTECs) of second phases in the 2xxx aluminum alloys: (a) LTEC along  $a$  or  $c$  principal axis, and its average by taking Al<sub>2</sub>Cu for example, the references [33,60,61] are also plotted in this sub-figure; (b) average LTEC of Al<sub>3</sub>Zr by considering different polymorphs with references [58,59]; (c) LTEC of all second phases versus temperature, and calculated results of pure Al from reference [58].

The specific heats at constant pressure ( $C_p$ ) and constant volume ( $C_V$ ) are two fundamental parameters, which can be related by [62]:

$$C_p - C_V = \lambda^2 V(T) T B \quad (10)$$

where  $\lambda$  refers to the volumetric TEC,  $V(T)$  and  $B$  are the volume and bulk modulus at temperature  $T$ . The results are plotted in Figure 7; Al<sub>3</sub>Cu<sub>2</sub>Fe has much higher heat capacity than other phases. At very low temperatures, all curves increase rapidly due to the crystalline lattice vibration, and then the increasing rate reduces slowly; for  $C_V$ , the curves tend to a well-known limit of Dulong-Petit, while for  $C_p$  the curves keep increasing due to the work done by lattice expansion.

Based on the curves of  $(F(V, T) - V)$ , the bulk modulus and its pressure derivative at different temperatures can be fitted based on Birch-Murnaghan EOS. The anti-compressibility of the second phases of 2xxx series aluminum alloys are given in Figure 8. At 0 K, Al<sub>3</sub>Fe, Al<sub>3</sub>Fe<sub>2</sub>Si, and Al<sub>7</sub>Cu<sub>2</sub>Fe are hard and anti-compressive, while Al<sub>2</sub>CuMg is the softest phase; meanwhile, three Al<sub>3</sub>Zr phases locate between them, which show moderate anti-compressibility. At temperatures of 300 or 700 K, the overall sequences of

second phases are similar;  $\text{Al}_2\text{CuMg}$  shows the most compressive character. However, with the increase of temperature,  $\text{Al}_2\text{Cu}$  becomes more and more soft, and its compressibility tends to be similar to the  $\text{Al}_2\text{CuMg}$  phase at 700 K.

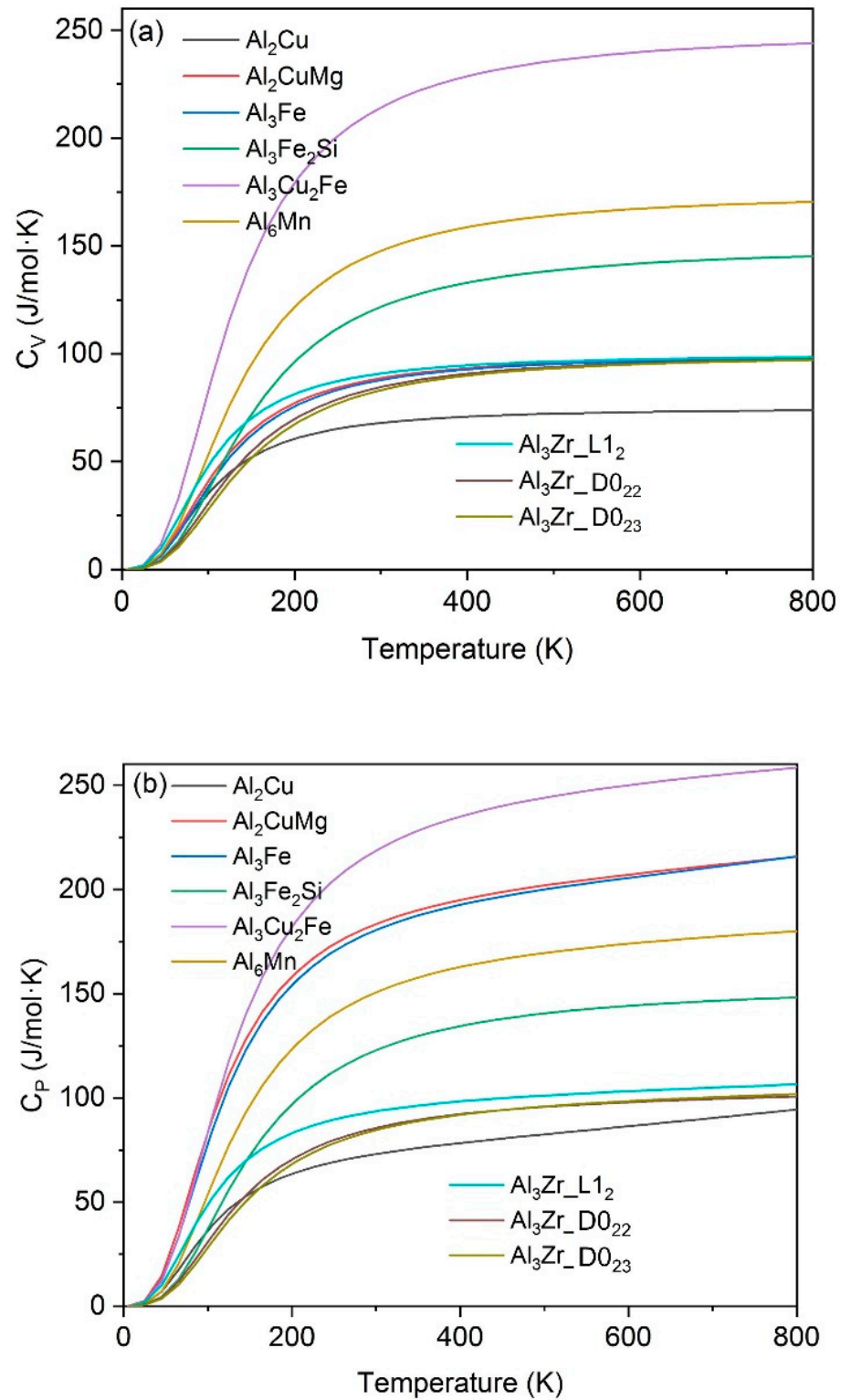


**Figure 7.** The specific heats at constant volume (a) or pressure (b) of second phases in the 2xxx aluminum alloys.

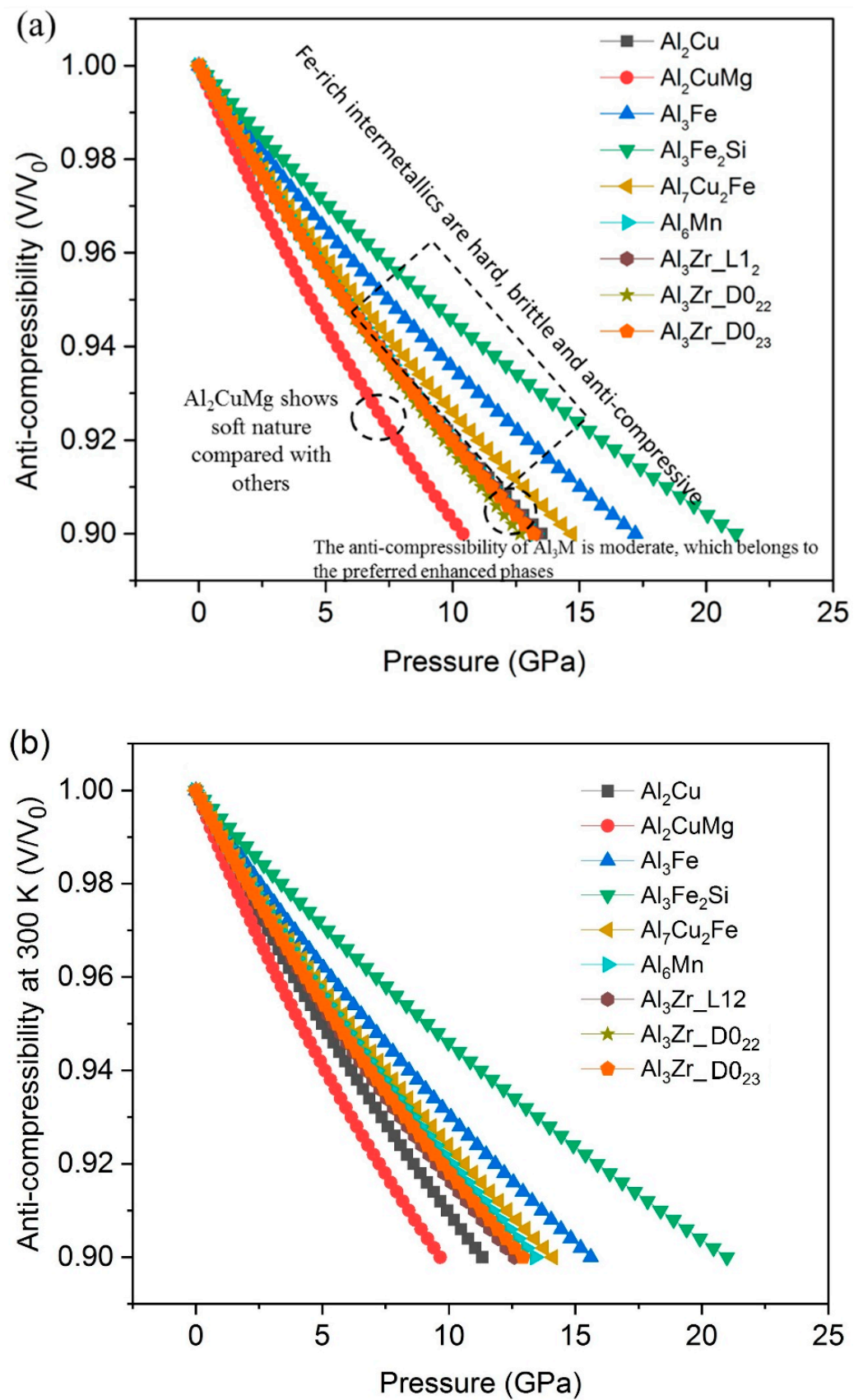
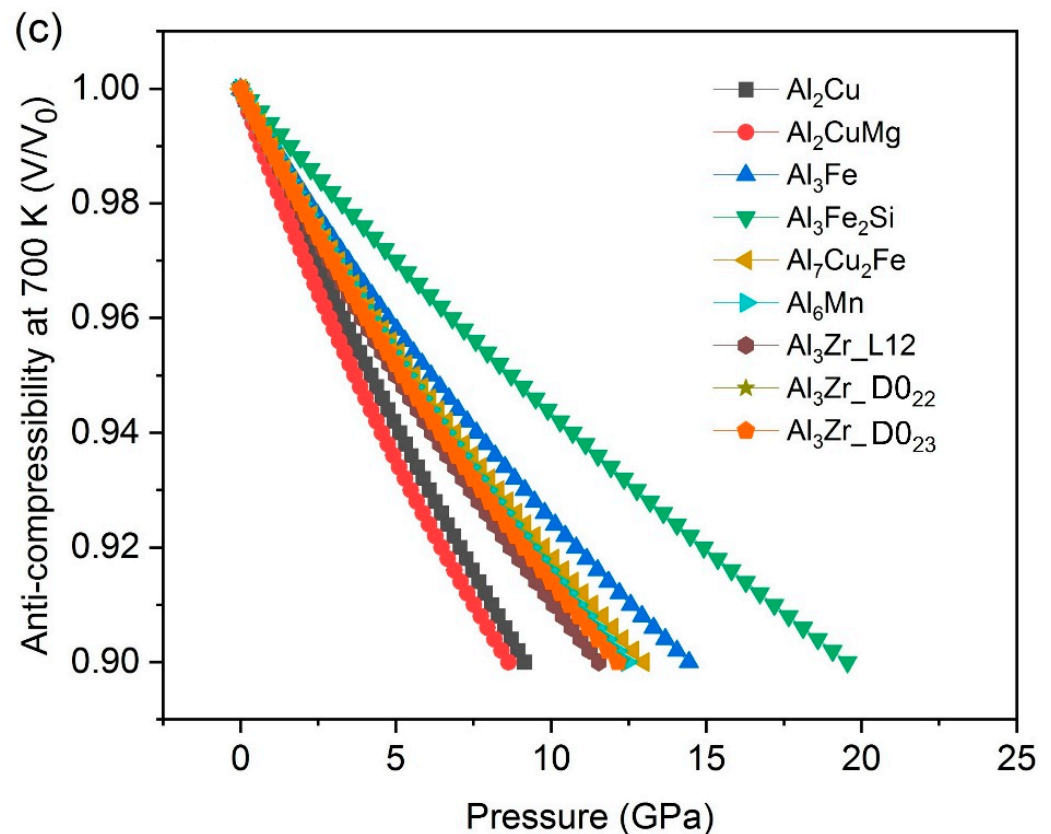


Figure 8. Cont.



**Figure 8.** The anti-compressibility of the second phases in the 2xxx aluminum alloys: (a) at 0 K, (b) at 300 K, and (c) at 700 K.

#### 4. Conclusions

Using first-principles calculations based on DFT, the structural stabilities, anisotropic mechanical, and thermophysical properties of precipitates of the 2xxx series aluminum alloys were investigated.

1. The calculated formation enthalpies are  $-0.151$ ,  $-0.17$ ,  $-0.16$ ,  $-0.463$ ,  $-0.02$ ,  $-0.266$ ,  $-0.195$ ,  $-0.489$ ,  $-0.464$ ,  $-0.461$ , and  $-0.181$  eV/atom for  $\text{Al}_2\text{Cu}$ ,  $\text{Al}_2\text{CuMg}$ ,  $\text{Al}_3\text{Fe}$ ,  $\text{Al}_3\text{Fe}_2\text{Si}$ ,  $\text{Al}_5\text{Cu}_2\text{Mg}_8\text{Si}_6$ ,  $\text{Al}_7\text{Cu}_2\text{Fe}$ ,  $\text{Al}_6\text{Mn}$ ,  $\text{Al}_3\text{Zr\_D0}_{23}$ ,  $\text{Al}_3\text{Zr\_D0}_{22}$ ,  $\text{Al}_3\text{Zr\_L1}_2$ , and  $\text{Al}_{20}\text{Cu}_2\text{Mn}_3$ , respectively.  $\text{Al}_5\text{Cu}_2\text{Mg}_8\text{Si}_6$  shows thermodynamic and mechanical unstable.
2. The bulk modulus of all precipitates are derived from 63.5 to 155.9 GPa, which has the trend of:  $\text{Al}_3\text{Fe}_2\text{Si} > \text{Al}_3\text{Fe} > \text{Al}_7\text{Cu}_2\text{Fe} > \text{Al}_6\text{Mn} \approx \text{Al}_3\text{Zr} \approx \text{Al}_{20}\text{Cu}_2\text{Mn}_3 > \text{Al}_2\text{Cu} > \text{Al}_2\text{CuMg} > \text{Al}_5\text{Cu}_2\text{Mg}_8\text{Si}_6$ . The results of  $B/G$  imply that  $\text{Al}_2\text{Cu}$  and  $\text{Al}_{20}\text{Cu}_2\text{Mn}_3$  are ductile precipitates. The hardness of  $\text{Al}_3\text{Zr\_D0}_{22}$  and  $\text{D0}_{23}$  phases is very high ( $\sim 18$  GPa); whereas  $\text{Al}_5\text{Cu}_2\text{Mg}_8\text{Si}_6$  shows low hardness value. The common precipitates of  $\text{Al}_2\text{Cu}$  and  $\text{Al}_2\text{CuMg}$  show a moderate hardness of 4.3 GPa and 6.8 GPa.
3. The thermal expansion characters are also calculated based on QHA;  $\text{Al}_2\text{CuMg}$  shows the highest LTEC, followed by  $\text{Al}_3\text{Fe}$ ,  $\text{Al}_2\text{Cu}$ ,  $\text{Al}_3\text{Zr\_L1}_2$  and others, while  $\text{Al}_3\text{Zr\_D0}_{22}$  is the lowest one; the discrepancy between  $\alpha$ -Al and  $\text{Al}_2\text{CuMg}$  is the smallest.
4. The results of compressibility indicate  $\text{Al}_3\text{Fe}$ ,  $\text{Al}_3\text{Fe}_2\text{Si}$  and  $\text{Al}_7\text{Cu}_2\text{Fe}$  are hard and anti-compressive, while  $\text{Al}_2\text{CuMg}$  is the softest one.

**Author Contributions:** Conceptualization, X.F., Y.L. and W.D.; formal analysis, X.F. and Y.L.; investigation, X.F., Q.Z. and J.G., writing-original draft preparation, X.F. and Y.L., supervision, X.F. and W.D., Methodology, Q.Z. and J.G., data curation, Y.Y., C.M., K.H., N.S., J.J., X.C. and H.W. All authors have read and agreed to the published version of the manuscript.

**Funding:** This work was funded by the National Key Research and Development Program of China (2021YFB3701204).

**Institutional Review Board Statement:** Not applicable.

**Informed Consent Statement:** Not applicable.

**Data Availability Statement:** Not applicable.

**Acknowledgments:** The authors wish to thank Y. Cheng from Xi'an Jiaotong University for providing CASTEP code support of this work.

**Conflicts of Interest:** The authors declare no conflict of interest.

## References

1. Bhuyan, M.; Borah, A. Investigating the effect of water cooling on hardness of 2xxx series aluminium alloy micro-alloyed with 0.02 and 0.04 wt% of Titanium. *Mater. Today Proc.* **2021**, *43*, 689–693. [[CrossRef](#)]
2. Kumar, N.S.; Dhruthi; Pramod, G.; Samrat, P.; Sadashiva, M. A Critical Review on Heat Treatment of Aluminium Alloys. *Mater. Today Proc.* **2022**, *58*, 71–79. [[CrossRef](#)]
3. Schuster, M.; De Luca, A.; Widmer, R.; Maeder, X.; Leinenbach, C. Processability, microstructure and precipitation of a Zr-modified 2618 aluminium alloy fabricated by laser powder bed fusion. *J. Alloys Compd.* **2022**, *913*, 165346. [[CrossRef](#)]
4. Kairy, S.; Rouxel, B.; Dumbre, J.; Lamb, J.; Langan, T.; Dorin, T.; Birbilis, N. Simultaneous improvement in corrosion resistance and hardness of a model 2xxx series Al-Cu alloy with the microstructural variation caused by Sc and Zr additions. *Corros. Sci.* **2019**, *158*, 108095. [[CrossRef](#)]
5. Moon, K.I.; Chang, K.Y.; Lee, K.S. The effect of ternary addition on the formation and the thermal stability of L1<sub>2</sub> Al<sub>3</sub>Zr alloy with nanocrystalline structure by mechanical alloying. *J. Alloys Compd.* **2000**, *312*, 273–283. [[CrossRef](#)]
6. Wang, S.C.; Starink, M.J. Precipitates and intermetallic phases in precipitation hardening Al-Cu-Mg-(Li) based alloys. *Inter-Natl. Mater. Rev.* **2005**, *50*, 193–215. [[CrossRef](#)]
7. Kertz, J.E.; Gouma, P.I.; Buchheit, R.G. Localized corrosion susceptibility of Al-Li-Cu-Mg-Zn alloy AF/C<sub>45</sub>8 due to interrupted quenching from solutionizing temperature. *Met. Mater. Trans. A* **2001**, *32*, 2561–2573. [[CrossRef](#)]
8. Feng, Z.; Yang, Y.; Huang, B.; Li, M.; Chen, Y.; Ru, J. Crystal substructures of the rotation-twinned T (Al<sub>20</sub>Cu<sub>2</sub>Mn<sub>3</sub>) phase in 2024 aluminum alloy. *J. Alloys Compd.* **2014**, *583*, 445–451. [[CrossRef](#)]
9. Shen, Z.; Liu, C.; Ding, Q.; Wang, S.; Wei, X.; Chen, L.; Li, J.; Zhang, Z. The structure determination of Al<sub>20</sub>Cu<sub>2</sub>Mn<sub>3</sub> by near atomic resolution chemical mapping. *J. Alloys Compd.* **2014**, *601*, 25–30. [[CrossRef](#)]
10. Huang, Y.-C.; Li, Y.; Xiao, Z.-B.; Szweczyk, R.; Yang, J. First-principles Study of Structure, Elastic and Electronic Properties of Precipitates Al<sub>3</sub>Fe, Al<sub>6</sub>Mn and Mg<sub>2</sub>Si in Al-Mg Alloys. In Proceedings of the 2nd Annual 2016 International Workshop on Materials Science and Engineering (IWMSE 2016), Guangzhou, China, 12–14 August 2016; pp. 876–883. [[CrossRef](#)]
11. Zhu, X.Z.; Dong, X.X.; Blake, P.; Ji, S.X. Improvement in as-cast strength of high pressure die-cast Al-Si-Cu-Mg alloys by syn-ergistic effect of Q-Al<sub>5</sub>Cu<sub>2</sub>Mg<sub>8</sub>Si<sub>6</sub> and θ-Al<sub>2</sub>Cu phases. *Mater. Sci. Eng. A* **2021**, *802*, 140612. [[CrossRef](#)]
12. Tian, J.; Zhao, Y.; Wen, Z.; Hou, H.; Han, P. Physical properties and Debye temperature of Al<sub>7</sub>Cu<sub>2</sub>Fe alloy under various pressures analyzed by first-principles. *Solid State Commun.* **2017**, *257*, 6–10. [[CrossRef](#)]
13. Kohn, W.; Sham, L.J. Self-consistent equations including exchange and correlation effects. *Phys. Rev.* **1965**, *140*, A1133–A1138. [[CrossRef](#)]
14. Segall, M.D.; Lindan, P.J.D.; Probert, M.J.; Pickard, C.J.; Clark, S.J.; Payne, M.C. First-principles simulation: Ideas, illustrations and the CASTEP code. *J. Phys. Condens. Matter* **2002**, *14*, 2717. [[CrossRef](#)]
15. Perdew, J.P.; Burke, K.; Wang, Y. Generalized gradient approximation for the exchange-correlation hole of a many-electron system. *Phys. Rev. B* **1996**, *54*, 16533–16539. [[CrossRef](#)]
16. Monkhorst, H.J.; Pack, J.D. Special points for Brillouin-zone integrations. *Phys. Rev. B* **1976**, *13*, 5188. [[CrossRef](#)]
17. Nielsen, O.H.; Martin, R.M. First-Principles Calculation of Stress. *Phys. Rev. Lett.* **1983**, *50*, 697–700. [[CrossRef](#)]
18. Kern, G.; Kresse, G.; Hafner, J. Ab initio calculation of the lattice dynamics and phase diagram of boron nitride. *Phys. Rev. B* **1999**, *59*, 8551. [[CrossRef](#)]
19. Baroni, S.; Giannozzi, P.; Isaev, E. Density-Functional Perturbation Theory for Quasi-Harmonic Calculations. *Rev. Miner. Geochem.* **2010**, *71*, 39–57. [[CrossRef](#)]
20. Blanco, M.A.; Francisco, E.; Luaña, V. GIBBS: Isothermal-isobaric thermodynamics of solids from energy curves using a quasi-harmonic Debye model. *Comput. Phys. Commun.* **2004**, *158*, 57–72. [[CrossRef](#)]
21. Birch, F. Finite Elastic Strain of Cubic Crystals. *Phys. Rev.* **1947**, *71*, 809–824. [[CrossRef](#)]
22. Huang, C.; Shao, H.B.; Ma, Y.L.; Huang, Y.C.; Xiao, Z.B. First-principles calculations of stability, electronic and elastic properties of the precipitates present in 7075 aluminum alloy. *Int. J. Mod. Phys. B* **2018**, *32*, 1850104. [[CrossRef](#)]
23. Zhang, J.; Huang, Y.N.; Mao, C.; Peng, P. Structural, elastic and electronic properties of θ (Al<sub>2</sub>Cu) and S (Al<sub>2</sub>CuMg) strengthening precipitates in Al-Cu-Mg series alloys: First-principles calculations. *Solid State Commun.* **2012**, *152*, 2100–2104. [[CrossRef](#)]

24. Li, C.M.; Zeng, S.M.; Chen, Z.Q.; Cheng, N.P.; Chen, T.X. First-principles calculations of elastic and thermodynamic properties of the four main intermetallic phases in Al–Zn–Mg–Cu alloys. *Comput. Mater. Sci.* **2014**, *93*, 210–220. [[CrossRef](#)]
25. Jain, A.; Ong, S.P.; Hautier, G.; Chen, W.; Richards, W.D.; Dacek, S.; Cholia, S.; Gunter, D.; Skinner, D.; Ceder, G.; et al. Commentary: The Materials Project: A materials genome approach to accelerating materials innovation. *APL Mater.* **2013**, *1*, 011002. [[CrossRef](#)]
26. Ouyang, Y.; Liu, F.; Lu, T.; Tao, X.; Du, Y.; He, Y. First-principles investigation of the mechanical, electronic and thermo-physical properties of Q-phase in Al–Mg–Si–Cu alloys. *Comput. Mater. Sci.* **2013**, *67*, 334–340. [[CrossRef](#)]
27. Zuo, L.; Ye, B.; Feng, J.; Kong, X.; Jiang, H.; Ding, W. Effect of Q-Al<sub>5</sub>Cu<sub>2</sub>Mg<sub>8</sub>Si<sub>6</sub> phase on mechanical properties of Al–Si–Cu–Mg alloy at elevated temperature. *Mater. Sci. Eng. A* **2017**, *693*, 26–32. [[CrossRef](#)]
28. Liu, Y.; Wen, J.C.; Zhang, X.Y.; Huang, Y.C. A comparative study on heterogeneous nucleation and mechanical properties of the fcc-Al/L1<sub>2</sub>-Al<sub>3</sub>M (M = Sc, Ti, V, Y, Zr, Nb) interface from first-principles calculations. *Phys. Chem. Chem. Phys.* **2021**, *23*, 4718. [[CrossRef](#)]
29. Yang, T.; Han, X.; Ding, Z.; Wang, Y.; Li, J. Electronic and structural properties of low-index L1<sub>2</sub>-Al<sub>3</sub>Zr surfaces by first-principle calculations. *Calphad* **2019**, *66*, 101645. [[CrossRef](#)]
30. Villars, P.; Calvert, L.D. *Pearson's Handbook of Crystallographic Data for Intermetallic Phases*; ASM: Cleveland, OH, USA, 1985.
31. Heying, B.; Hoffmann, R.D.; Pöttgen, R. Structure Refinement of the S-Phase Precipitate MgCuAl<sub>2</sub>. *Z. Für Nat. B* **2005**, *60*, 491–494. [[CrossRef](#)]
32. Bown, M.G.; Brown, P.J. The structure of FeCu<sub>2</sub>Al<sub>7</sub> and T (CoCuAl). *Acta Crystallogr.* **1956**, *9*, 911–914. [[CrossRef](#)]
33. Mondolfo, L. *Aluminum Alloys, Structure and Properties*; Butterworth: London, UK, 1976.
34. Ryum, N. Precipitation and recrystallization in an Al-0.5 WT% Zr-alloy. *Acta Metall.* **1969**, *17*, 269–278. [[CrossRef](#)]
35. Desch, P.; Schwarz, R.; Nash, P. Formation of metastable L1<sub>2</sub> phases in Al<sub>3</sub>Zr and Al-12.5%X-25%Zr (X ≡ Li, Cr, Fe, Ni, Cu). *J. Less Common Met.* **1991**, *168*, 69–80. [[CrossRef](#)]
36. Nicol, A.D.I. The structure of MnAl<sub>6</sub>. *Acta Crystallogr.* **1953**, *6*, 285–293. [[CrossRef](#)]
37. Kontio, A.; Coppens, P. New study of the structure of MnAl<sub>6</sub>. *Acta Crystallogr.* **1981**, *B37*, 433–435. [[CrossRef](#)]
38. Panda, K.; Chandran, K.R. First principles determination of elastic constants and chemical bonding of titanium boride (TiB) on the basis of density functional theory. *Acta Mater.* **2006**, *54*, 1641–1657. [[CrossRef](#)]
39. Hill, R. The Elastic Behaviour of a Crystalline Aggregate. *Proc. Phys. Soc. Sect. A* **1952**, *65*, 349. [[CrossRef](#)]
40. Patil, S.K.R.; Khare, S.V.; Tuttle, B.R.; Bording, J.D. Kodambaka, Mechanical stability of possible structures of PtN investigated using first-principles calculations. *Phys. Rev. B* **2006**, *73*, 104118. [[CrossRef](#)]
41. Wu, Z.J.; Zhao, E.J.; Xiang, H.P.; Hao, X.F.; Liu, X.J. Meng, Crystal structures and elastic properties of superhard IrN<sub>2</sub> and IrN<sub>3</sub> from first principles. *J. Phys. Rev. B* **2007**, *76*, 054115. [[CrossRef](#)]
42. Hu, H.; Zhao, M.Q.; Wu, X.Z.; Jia, Z.H.; Wang, R.; Li, W.G.; Liu, Q. The structural stability, mechanical properties and stacking fault energy of Al<sub>3</sub>Zr precipitates in Al–Cu–Zr alloys: HRTEM observations and first-principles calculations. *J. Alloys Compd.* **2016**, *681*, 96–108. [[CrossRef](#)]
43. Zhou, W.; Liu, L.; Li, B.; Song, Q.; Wu, P. Structural, Elastic, and Electronic Properties of Al–Cu Intermetallics from First-Principles Calculations. *J. Electron. Mater.* **2008**, *38*, 356–364. [[CrossRef](#)]
44. Zhang, G.W.; Sun, F.; Liu, H.P.; Ren, X.Y.; Xu, H.; Wang, M.J.; Fu, Y.Z. Exploration of D022-Type Al<sub>3</sub>TM (TM=Sc, Ti, V, Zr, Nb, Hf, Ta): Elastic Anisotropy, Electronic Structures, Work Function and Experimental Design. *Materials* **2021**, *14*, 2206. [[CrossRef](#)] [[PubMed](#)]
45. Tian, T.; Wang, X.; Li, W. Ab initio calculations on elastic properties in L1<sub>2</sub> structure Al<sub>3</sub>X and X<sub>3</sub>Al-type (X=transition or main group metal) intermetallic compounds. *Solid State Commun.* **2013**, *156*, 69–75. [[CrossRef](#)]
46. Ringer, S.P.; Sofyan, B.T.; Prasad, K.S.; Quan, G.C. Precipitation reactions in Al–4.0Cu–0.3Mg (wt.%) alloy. *Acta Mater.* **2008**, *56*, 2147–2160. [[CrossRef](#)]
47. Herper, H.C.; Hoffmann, E.; Entel, P. Ab initio full-potential study of the structural and magnetic phase stability of iron. *Phys. Rev. B* **1999**, *60*, 3839. [[CrossRef](#)]
48. Bannikov, V.V.; Shein, I.R.; Ivanovskii, A.L. Electronic structure, chemical bonding and elastic properties of the first thorium-containing nitride perovskite TaThN<sub>3</sub>. *Phys. Status Solidi (RRL)* **2007**, *1*, 89–91. [[CrossRef](#)]
49. Chen, X.Q.; Niu, H.Y.; Li, D.Z.; Li, Y.Y. Modeling hardness of polycrystalline materials and bulk metallic glasses. *Intermetallics* **2011**, *19*, 1275–1281. [[CrossRef](#)]
50. Westbrook, J.H.; Fleischer, R.L. *Basic Mechanical Properties and Lattice Defects of Intermetallic Compounds*; Wiley: New York, NY, USA, 2000.
51. Shang, S.; Wang, J.; Wang, Y.; Du, Y.; Liu, Z. Phonon and thermodynamic properties of Al–Mn compounds: A first-principles study. *Comput. Mater. Sci.* **2011**, *50*, 2096–2103. [[CrossRef](#)]
52. Wang, S.C.; Starink, M.J. The assessment of GPB<sub>2</sub>/S'' structures in Al–Cu–Mg alloys. *Mater. Sci. Eng. A* **2004**, *386*, 156–163. [[CrossRef](#)]
53. Nye, J.F. *Physical Properties of Crystals*; Oxford University Press: Oxford, UK, 1985.
54. Ranganathan, S.I.; Ostoja-Starzewski, M. Universal Elastic Anisotropy Index. *Phys. Rev. Lett.* **2008**, *101*, 055504. [[CrossRef](#)]
55. Feng, J.; Xiao, B.; Zhou, R.; Pan, W. Anisotropy in elasticity and thermal conductivity of monazite-type REPO<sub>4</sub> (RE= La, Ce, Nd, Sm, Eu and Gd) from first-principles calculations. *Acta Mater.* **2013**, *61*, 7364–7383. [[CrossRef](#)]

56. Anderson, O.L. A simplified method for calculating the debye temperature from elastic constants. *J. Phys. Chem. Solids* **1963**, *24*, 909–917. [[CrossRef](#)]
57. Manghnani, M.H.; Fisher, E.S.; Brower, W.S.J. Temperature dependence of the elastic constants of single-crystal rutile between 4° and 583°K. *J. Phys. Chem. Solids* **1972**, *33*, 2149–2159. [[CrossRef](#)]
58. Saha, S.; Todorova, T.Z.; Zwanziger, J.W. Temperature dependent lattice misfit and coherency of Al<sub>3</sub>X (X=Sc, Zr, Ti and Nb) particles in an Al matrix. *Acta Mater.* **2015**, *89*, 109–115. [[CrossRef](#)]
59. Gautam, G.; Kumar, N.; Mohan, A.; Mohan, S.; Singh, D. ZrB<sub>2</sub> nanoparticles transmuting tribological properties of Al<sub>3</sub>Zr/AA5052 composite. *J. Braz. Soc. Mech. Sci. Eng.* **2019**, *41*, 469. [[CrossRef](#)]
60. Ozolins, V.; Wolverton, C. Entropically Favored Ordering: The Metallurgy of Al<sub>2</sub>Cu Revisited. *Phys. Rev. Letters.* **2001**, *86*, 5518–5521. [[CrossRef](#)]
61. Lokker, J.P.; Van Der Pers, N.M.; Verbruggen, A.H.; Janssen, G.C.A.M.; Jongste, J.F.; Radelaar, S. Localized stress near and the thermal expansion of Al<sub>2</sub>Cu precipitates in an Al thin film matrix. *J. Appl. Phys.* **2000**, *87*, 682–688. [[CrossRef](#)]
62. Grimval, G. *Thermophysical Properties of Materials*; North Holland: Amsterdam, Netherlands, 1999.